






## Experimental and Numerical Studies on Flexural Behavior of GGBS-Based Geopolymer Ferrocement Beams

Taha A. El-Sayed <sup>1\*</sup>, Ahmed F. Deifalla <sup>2</sup>, Yousry B. Shaheen <sup>3</sup>,  
Hossam H. Ahmed <sup>1</sup>, Aya K. Youssef <sup>1</sup>

<sup>1</sup> Department of Structural Engineering, Shoubra Faculty of Engineering, Benha University, Cairo 11629, Egypt.

<sup>2</sup> Department of Structural Engineering and Construction Management, Future University in Egypt, New Cairo City 11835, Egypt.

<sup>3</sup> Department of Structural Engineering, Faculty of Engineering, Menoufia University, Shebin El Koum, Egypt.

Received 05 December 2022; Revised 23 February 2023; Accepted 26 February 2023; Published 01 March 2023

### Abstract

The ferrocement structural concept has been shown to offer exceptional mechanical properties in terms of toughness, fracture control, and impact resistance, which are achieved by tight spacing and homogeneous reinforcement dispersion within the matrix. The flexure behavior of geopolymer ferrocement beams under axial flexural stress is being explored experimentally and computationally in this present work. Under flexural loads, nine samples of geopolymer ferrocement beams 150 mm thick, 75 mm wide, and 1700 mm long were tested to failure. The reinforcing steel bars and wire meshes, as well as the quantity of wire mesh layers, were the key factors studied. The initial crack load, ultimate failure load, and mid-span deflection with various loading phases, cracking patterns, energy absorption, and ductility index were all studied in relation to the behavior. In terms of carrying capacity, absorbing energy, and ductility, welded steel wire mesh beams fared better than other materials. Using ANSYS-19 software, nonlinear finite element analysis (NLFEA) was carried out to demonstrate the behavior of composite ferrocement geopolymer beams. The ensuing experimental and numerical data demonstrated that the degree of experimental value estimation supplied by the FE simulations was sufficient. It is crucial to demonstrate that, in comparison to control specimens, the increase in strength of specimens reinforced with tensar meshes was reduced by around 15%.

**Keywords:** Ground Granulated Blast-Furnace Slag (GGBS); Geopolymer Concrete; Wire Meshes; Finite Element Analysis (FEA).

## 1. Introduction

Ferrocement had lately become a popular new building material. According to ACI, ferrocement is a form of reinforced concrete that is frequently made of cement paste and reinforced with thin layers of mesh that have tiny wire diameters. The mesh might be created from metal or any other appropriate material. The openness and tightness of the reinforcing system it is intended to envelop should be consistent with the fineness of the mortar matrix and its composition. It's possible for the matrix to have irregular fibers [1–2]. The results of an experimental investigation into the viability of using prefabricated concrete ferrocement as an absorption cover layer to the consequently poured in situ reinforced concrete components located in environments in which there is a significant risk of corrosion of steel reinforcement were presented by Mays and Barnes [3]. The development of composite structural behavior was a special goal of the research, along with developing an appropriate and long-lasting link between the ferrocement layer and the concrete core. They concluded that permanent ferrocement formwork provided a 15% increase in strength over

\* Corresponding author: [taha.ibrahim@feng.bu.edu.eg](mailto:taha.ibrahim@feng.bu.edu.eg)

 <http://dx.doi.org/10.28991/CEJ-2023-09-03-010>



© 2023 by the authors. Licensee C.E.J, Tehran, Iran. This article is an open access article distributed under the terms and conditions of the Creative Commons Attribution (CC-BY) license (<http://creativecommons.org/licenses/by/4.0/>).

conventionally reinforced concrete, in addition to improving the resistance to chloride penetration by using Styrene Butadiene Rubber (SBR) or an acrylic bond coat between the ferrocement forms and the concrete. Abdul Kadir et al. [4] presented the findings of a flexural behavior test on RC beams reinforced with ferrocement permanent formwork. One of the beams has no structural shear connection between ferrocement forms and the cement matrix. The other had eight beams with shear connections formed as  $12 \times 22$  mm rectangular humps at every 22 mm center.

The steel mesh area was kept constant at  $55 \text{ mm}^2$  for all beams, whereas the area of reinforcing bars in the concrete core varied. Under two-point load testing, the reinforced concrete beams with ferrocement structural material collapsed due to flexure. Depending on the amount of steel and the application of shear connections, the ferrocement formwork-incorporated beams increased the flexural strength of the composite beams by 16 to 75%. When compared to forms without shear connections, the ferrocement forms with reinforced concrete cores had an average 10% stronger strength, but they also displayed reduced deflections under the same load. Fahmy et al. [5] conducted research in which twelve ferrocement hollow core panels and sandwich panels were constructed and tested for usage in slabs, walls, and roofing systems. Sandwich panels were constructed with two outer ferrocement skins separated by a light-weight core. As core materials, lightweight brick and foam concrete were investigated. The hollow cored panels had three circular holes running the length of the specimen and were made from the same mortar matrix as the skin ferrocement layer. In terms of behavior, the light brick specimens outperformed the foam concrete core specimens in this investigation. The results also showed that the proposed panels had high ultimate and serviceability loads, fracture resistance management, high ductility, and excellent energy absorption properties.

For thin radial gates with high strength, fracture resistance, flexibility, and energy absorption suitable for irrigation operations, ferrocement is proposed to replace the commonly used steel gages. This paper presents the results of an analytical study of the strength of a proposed ferrocement radial gate. The cement-sand matrix of the ferrocement composite was designed to offer superior tensile, flexural, and compressive strength for the ferrocement radial gates. This was done by replacing a part of the concrete mixture with silica fume. An experimental investigation into the impact of silica fume on matrix strength discovered that, for a water-binder ratio of 0.28, substituting 15% of the cement with silica fume was the ideal amount. Fahmy et al. [6] studied the tensile strength of 12.5 mm thick thin Ferrocement plates, looking at the influence of characteristics such as mesh form, specific surface, volume fraction, mesh yield strength, and skeleton bars. The specimens were specially designed to assure gauge length failure. For excellent workability, high strength, and high durability, the matrix was proportioned with a low water to binder ratio and 50% cement substitution with fly ash. Cracking and distortion were monitored throughout the loading history. The results demonstrated that a single complex relationship could describe the composite properties of elastic modulus and strength characteristics exceedingly well; however, there was a substantial connection between the composite properties' ultimate flexural strength and ultimate tensile strength. High-strength ferrocement sheets with good fracture resistance may be developed for a wide variety of structural purposes, especially with adequate reinforcement and matrix design.

According to Swamy & Shaheen [7], the experimental results of previous research were used to fabricate ferrocement sandwich wall carrying units that may be employed as wall bearings. Sandwich panels were constructed from two thin layers of ferrocement reinforced by one or two layers of tightly packed welded wire mesh. The core of the panel was made of lightweight brick. Shear connectors constructed of Z-shaped steel bars were used to transfer shear here between two ferrocement skin layers. The shear connections were installed in the brick-mortar joints and connected to the ferrocement skin layer's mesh reinforcement. Single- and double-layer metal meshes with a 10 mm layer thickness were used. The core material had a thickness of 100 mm. In the experiment, eight sandwich panels were evaluated. The results of the tests demonstrated that the kind of steel mesh, panel thickness, and number of reinforcing meshes all had a major impact on the panel's behavior. According to the results, all tested panels demonstrated good energy absorption capabilities, high serviceability and ultimate loads, high ductility, and fracture resistance control. Lately, ferrocement has sparked interest in developing countries as a potential construction material, notably for residential roofing [8]. Joshi [9] examined the axial stress behavior and strength of wall components. Ferrocement displayed exceptional toughness, fracture control, and impact strength as a construction material, due to the material's tight spacing and homogenous reinforcement dispersion. Many researchers have researched this material's mechanical and physical properties, and diverse test results are available to define its design and construction performance criteria [10–22].

### 1.1. Research Significance

The main objective of this study is to examine how different wire meshes affect the behavior of RC beams made of geopolymer ferrocements based on GGBS. For this objective, an experimental design was created, and ANSYS 2019-R1 was used to construct a finite element prototype. Nine samples of 150 mm in height, 75 mm in width, and 1700 mm in length of geopolymer ferrocement beams were evaluated under flexural pressure to failure. The wire meshes, reinforcing steel bars, and number of wire mesh layers are the variables in this study. The process and methodology of the workflow are presented in Figure 1.

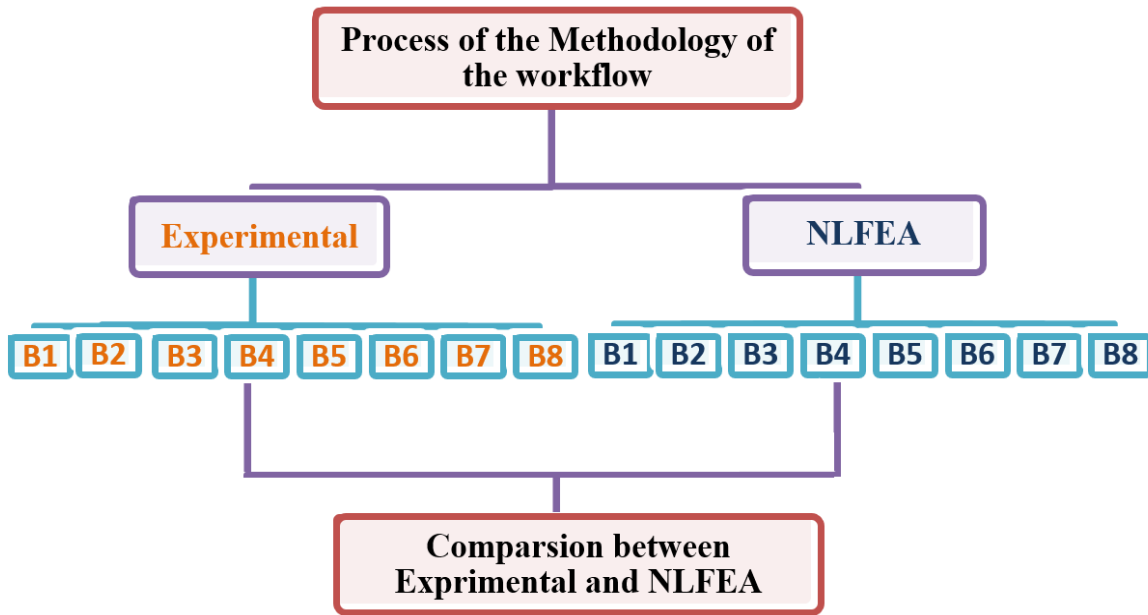


Figure 1. Grading curve for the fine aggregate

## 2. Experimentation

As indicated in Figure 2, universal testing equipment with a maximum capacity of 2000 kN was used to test the beam samples that were subjected to four points of loading with 1700 mm length and 400 mm gap between loads. The major purpose of this study was to evaluate the ultimate load capacity, ultimate deflection, and failure mechanism of GGBS geopolymer concrete beams.

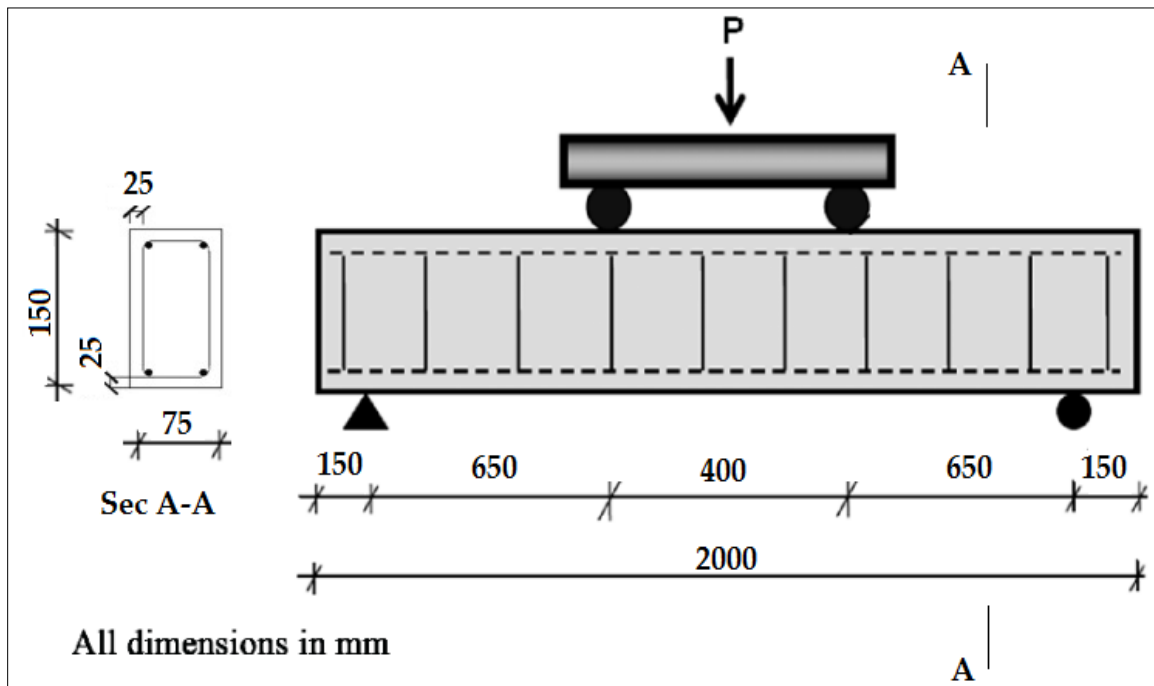


Figure 2. Beams concrete dimensions & RFT details

### 2.1. Utilized Materials

#### 2.1.1. Fine Aggregate

Fine aggregate with a specific gravity of 2.55 and a bulk density of 1780 kg/m<sup>3</sup> was obtained from a nearby source for this project. Egypt Specification ECP 203-2020 [23] was used to conduct the sieve analysis. Figure 3 depicts the grade.

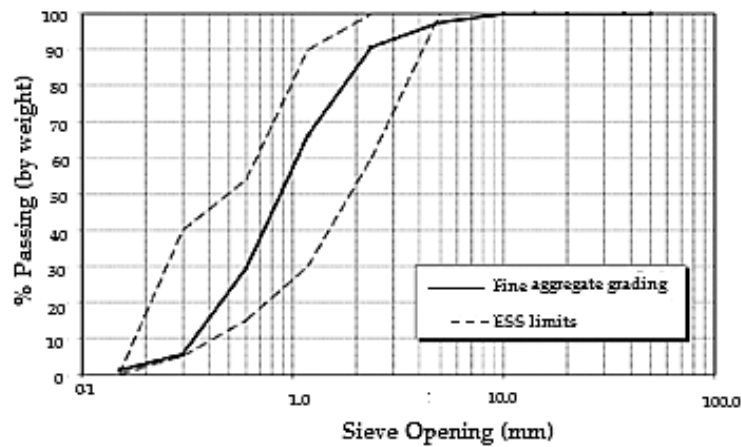


Figure 3. Grading curve for the fine aggregate

**2.1.2. Coarse Aggregate**

Crushed limestone aggregate from a nearby quarry with a maximum nominal size of 9 mm (as indicated in Figure 4), a specific gravity of 2.60, and a bulk density of 1750kg/m<sup>3</sup>. 9 mm collective absorption was 1.1 percent. The absorption values were fewer than the allowable maximum of 2.5 percent, according to Egypt Specification ECP 203-2020 [23]. Figure 5 depicts the grade.



Figure 4. 9 mm aggregate size

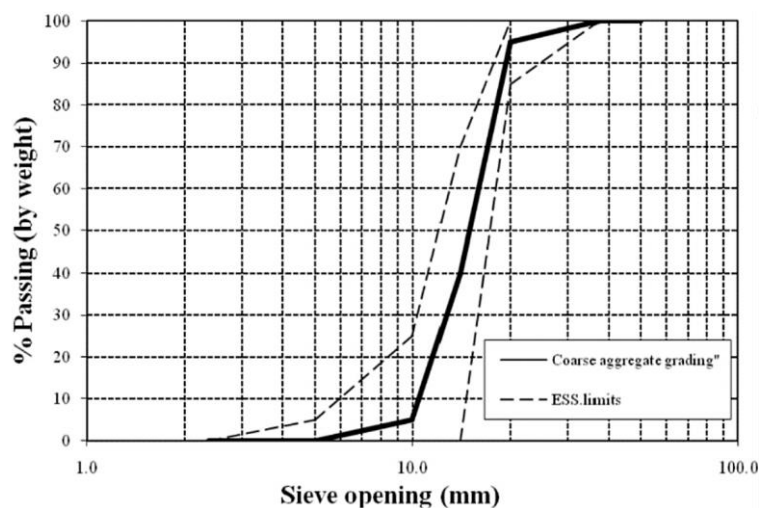


Figure 5. Grading curve for the coarse aggregate

**2.1.3. Ground Granulated Blast-Furnace Slag “GGBS”**

Ground granulated blast-furnace slag is a glassy granular dark-grey solid, as seen in Figure 6. It is a non-metallic compound composed of silicon, calcium, and various bases. The GGBS used had a specific gravity of 2.91 g/cm<sup>2</sup> and a surface area of 5200 cm<sup>2</sup>/g.



Figure 6. Ground Granulated Blast-furnace Slag (GGBS)

**2.1.4. Water**

Water utilized in mixing and curing.

**2.1.5. Alkaline Activator**

Sodium meta-silicate (Na<sub>2</sub>SiO<sub>3</sub>) and sodium hydroxide (NaOH) were the alkaline activators utilized in this work [17].

**2.1.6. Reinforced Steel Bars**

Two different kinds of reinforcing steel from the El-Dekhiela plant in Egypt were used. Type I: 24/35 (simple bars), 6 mm in diameter; Type II: 36/52 (deformed bars), 12 and 10 mm in diameter.

**2.1.7. Steel Wire Meshes**

*Expanded & Welded Wire Mesh*

The various types of ferrocement meshes used in this study were displayed in Figure 7. Table 1 shows the properties of expanded and welded wire meshes [10].

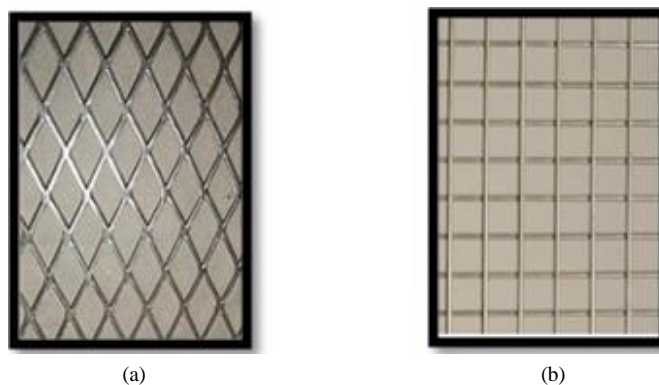


Figure 7. Mesh types include a) expanded wire mesh, b) welded wire mesh

Table 1. The mechanical characteristics of expanded and welded wire mesh

Expanded Wire Mesh		Welded Wire Mesh	
Dimension size	16×31 mm	Dimension size	12.5×12.5 mm
Weight	1660 gm/m <sup>2</sup>	Weight	600 gm/m <sup>2</sup>
Sheet Thickness	1.25 mm	Wire Diameter	0.7 mm
Young's Modulus	12000 N/mm <sup>2</sup>	Young's Modulus	17000 N/mm <sup>2</sup>
Yield Stress	250 N/mm <sup>2</sup>	Yield Stress	400 N/mm <sup>2</sup>
Yield Strain	9.7×10 <sup>-3</sup>	Yield Strain	1.7×10 <sup>-3</sup>
Ultimate Strength	380 N/mm <sup>2</sup>	Ultimate Strength	600 N/mm <sup>2</sup>
Ultimate Strain	59.2×10 <sup>-3</sup>	Ultimate Strain	58.8×10 <sup>-3</sup>

### Polyethylene (Tensar) Mesh

This mesh is made from high-density polyethylene. As shown in Figure 8, a "Geogrid CE 121" with an aperture size of 6×8 mm, thickness of 3.3 mm, weight of 725 gm/m<sup>2</sup>, and volume fraction of 2.04 percent was used.

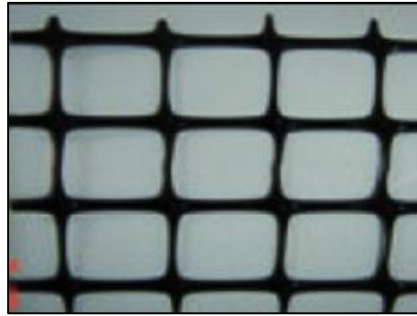


Figure 8. Polyethylene (Tensar) mesh

### Fiberglass Mesh

The Gavazzi "V3-133-A" with a 12.5×11.5 mm hole was used. The cross-section dimension of the fiberglass in the longitudinal direction is 1.66×0.66 mm and, in the transverse, direction is 1.0×0.5 mm, as shown in Figure 7. The mesh weighs 123 grammes per square meter and has a volume fraction of 0.535 %.

## 2.2. Mixture Design

The design mix was predicted to have a (fcu) of 50 MPa after 28 days. The blend's qualities are shown in Table 2.

Table 2. Concrete mix design

Item	GGBS (kg/m <sup>3</sup> )	Coarse aggregate (kg/m <sup>3</sup> )	Fine aggregate (kg/m <sup>3</sup> )	GGBS (kg/m <sup>3</sup> )	NaOH (kg/m <sup>3</sup> )	Na <sub>2</sub> SiO <sub>3</sub> (kg/m <sup>3</sup> )	Water (kg/m <sup>3</sup> )
Per m <sup>3</sup> of concrete	400	1150	650	40	50	150	47

## 2.3. Beams Specimens' Description

The purpose of the experimental inquiry was to ascertain how geopolymer RC beams behave generally, how they fracture, and how much weight they can ultimately support. Nine geopolymer ferrocement RC beams with dimensions of 75 × 150 × 1700 mm were included in the experimental design and were reinforced with steel bars (212 in tension and 210 in compression). Under four lines of strain, beams were evaluated using 2000 kN of universal compression testing equipment. After 28 days, the concrete mix for the beams was intended to reach fcu=50MPa. Figure 2 shows the concrete dimensions and RFT information of the tested beams. All beam samples are included in Table 3. Figure 9 presents the tested beam reinforcement configurations.

Table 3. Notation for tested beams

Series	Specimen ID	Specimens' description	Volume of Fraction	Bottom RFT.	Top RFT.	Stirrups
Control	B1	Control	-	2φ12	2φ10	10φ6
Group A: Welded wire mesh	B1-A	One-layer welded	0.00270	2φ12	2φ10	3φ6
	B2-A	Two-layers welded	0.00540	2φ12	2φ10	3φ6
	B3-A	Three-layers welded	0.00810	2φ12	2φ10	3φ6
Group B: Expanded wire mesh	B4-B	One-layer expanded	0.00573	2φ12	2φ10	3φ6
	B5-B	Two-layers expanded	0.01510	2φ12	2φ10	3φ6
Group C: Tensar mesh	B6-C	One-layer Tensar	0.02040	2φ12	2φ10	3φ6
Group D: Fiberglass mesh	B7-D	One-layer fiber glass	0.00535	2φ12	2φ10	5φ6
	B8-D	Two-layers fiber glass	0.01070	2φ12	2φ10	3φ6





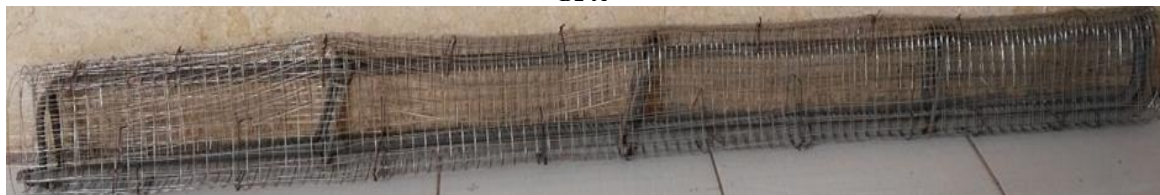
B1



B1-A



B2-A



B3-A



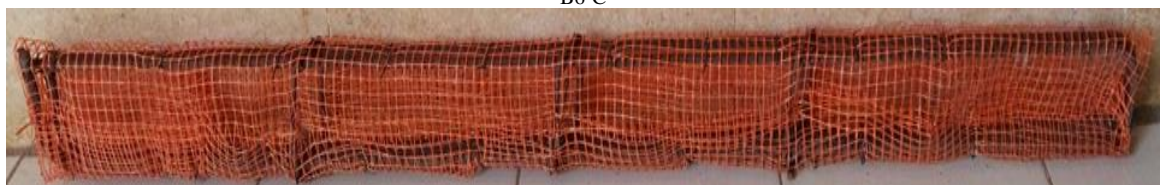
B4-B



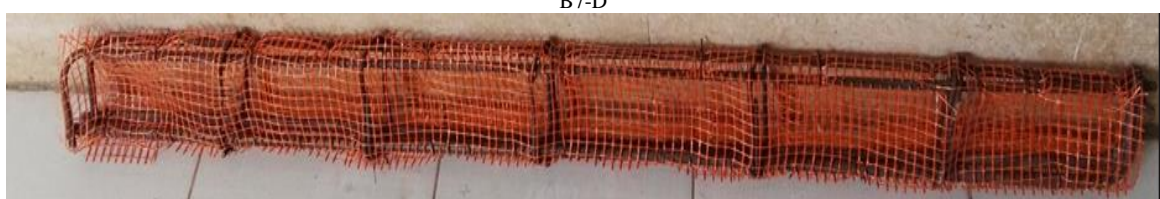
B5-B



B6-C



B7-D



B8-D

Figure 9. Configurations of reinforced beams tested

### 2.4. Test Setup

All beams exposed to two-point loadings were examined using testing equipment with a maximum capacity of 2000 kN. Figure 10 depicts beam parameters with a 1400 mm effective span and a load distance of 300 mm. The L.V.D.T. equipment was used to measure the center deflections of all tested beams until they failed.

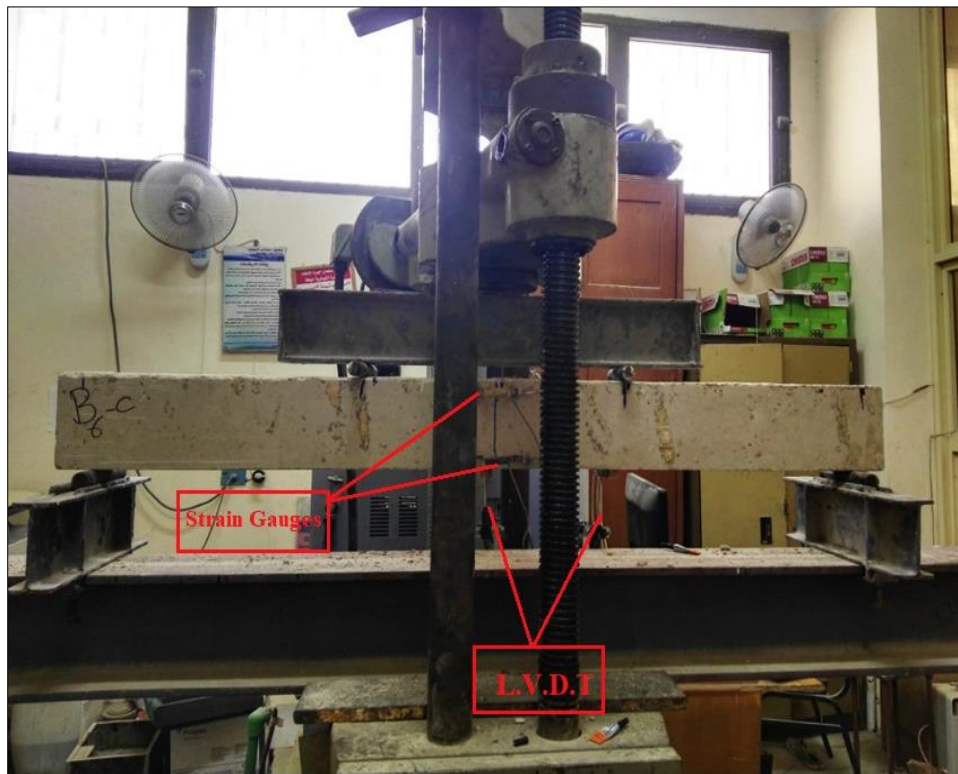


Figure 10. Test Setup

### 3. Discussion of Experiment Results

The next sections demonstrate and describe the behavior of the test specimens in terms of ultimate load, ultimate deflection, load-deflection relationship, cracking behavior, load-strain relationship, and mechanism of failure.

#### 3.1. Ultimate Load

Table 4 shows the ultimate loads for the tested beams. Control B1 has an ultimate load of 59.0 kN. The ultimate loads of group A, beams B1-A to B3-A, ranged from 37.8 kN to 43.7 kN. The ultimate loads for group B, beams B4-B and B5-B, are 33.5 kN and 40.7 kN, respectively. The ultimate load of the modelled beams was enhanced by using both fibers. Beam B6-C for group C, having a maximum load of 50.0 kN. The ultimate loads for group D, beams B7-D and B8-D, were 31.0 kN and 37.5 kN, respectively.

Table 4. Experimental results

Beam no.	First crack load (kN)	Service load (kN)	Ultimate load (kN)	Def. at first crack load (mm)	Def. at Ult. load (mm)	Ductility ratio	Energy Absorption (kN.mm)
B1	42.0	36.50	59.0	2.40	3.59	1.49	201.66300
B1-A	27.0	23.27	37.8	2.35	3.37	1.43	84.710200
B2-A	19.0	24.20	39.3	2.53	4.70	1.85	103.39800
B3-A	22.5	26.90	43.7	1.95	5.58	2.86	225.77300
B4-B	20.0	20.58	33.5	2.24	3.40	1.51	69.79200
B5-B	24.0	25.08	40.7	3.12	5.75	1.84	125.80200
B6-C	23.0	30.89	50.0	1.90	4.50	2.36	124.30340
B7-D	15.0	19.00	31.0	1.56	3.10	1.98	46.48300
B8-D	22.0	23.00	37.5	2.10	3.70	1.76	86.44017



### 3.2. Ultimate Deflection

The ultimate deflection for all tested beams is shown in Table 4. The control B1 had a center deflection of 3.59 mm. The greatest central deflection for group A varied from 3.37 to 5.58 mm for beams B1-A to B3-A, which were more than that of control B1. The greatest central deflection at ultimate load for beams B4-B and B5-B in group B was 3.40 mm and 5.75 mm, respectively, which is likewise more than that of control beam B2. Beam B6-C for group C, having an ultimate deflection of 4.50 mm. The ultimate deflections for group D, beams B7-D and B8-D, were 3.10 mm and 3.70 mm, respectively.

### 3.3. Load-Deflection Relationship

Figure 11 depicts the connection between the applied load and the center deflection for the tested beams. This chart clearly shows that the connection between load and deflection may be separated into three stages for all specimens, as follows:

- Elastic behavior before the first crack. In this stage, the load-deflection relationship is linear. The slope of the load deflection curve at this step varies depending on the type of test specimen used. The divergence from linearity marks the conclusion of this stage. The amount of this step varied according to the test settings;
- The slope of the load-deflection curve gradually changes in the second stage due to the expected drop in the stiffness of the specimen as a result of serial cracks;
- Substantial plastic deformation occurred in the third stage as a result of the reinforcing bars yielding and the large expansion in the reinforcing mesh of the ferrocement beams.

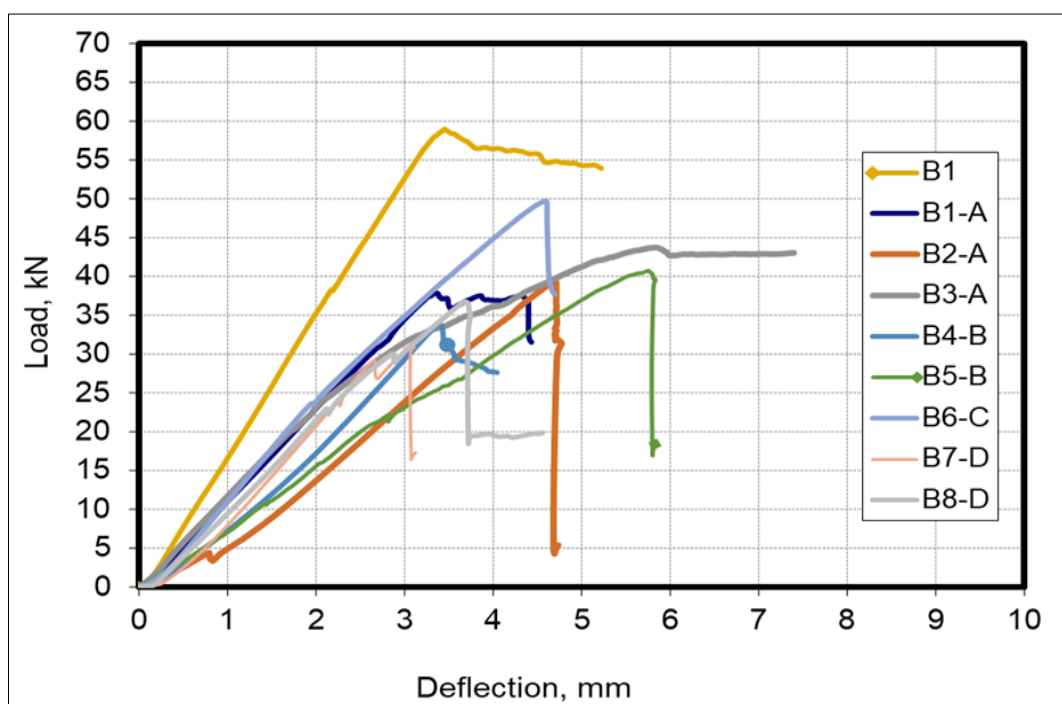


Figure 11. Load deflection curves for all beams

Table 4 shows the behavior of all test specimens in terms of the deflection at ultimate load, the service load, the first crack load, the ductility ratio, and the energy absorption. During the test, the deflection at ultimate, the first crack load, and the ultimate load were acquired, while the service load, the energy absorption, and the ductility ratio were calculated using the load-deflection behavior for each specimen. The first fracture load was calculated from the load deflection curve at the point when it began to depart from the linear relationship. In this study, the load corresponding to a deflection equal to  $\text{span}/250$  was taken as the service load (i.e., the flexural serviceability load).

The present part illustrates the comparison of the behavior of the tested beam up to failure as acquired from the experimental data. The comparison of all tested beams in terms of load-deflection relationship is presented in Figures 12 to 17, which show the serviceability load, the first crack load, the ultimate load and corresponding deflection, the energy absorption, and the ductility ratio for all tested beams.

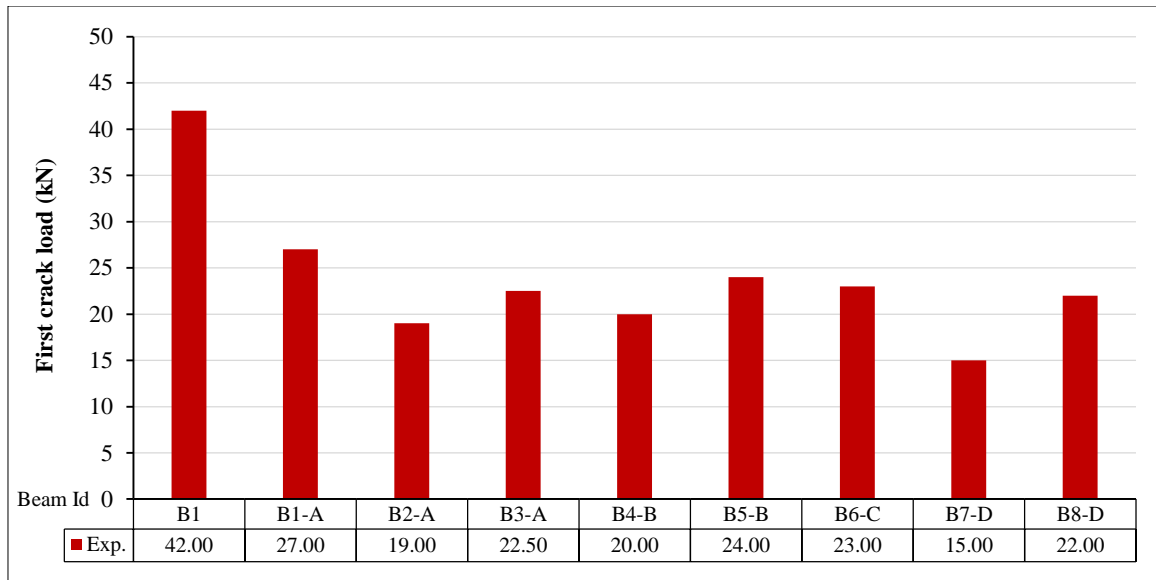


Figure 12. First crack load for tested beams

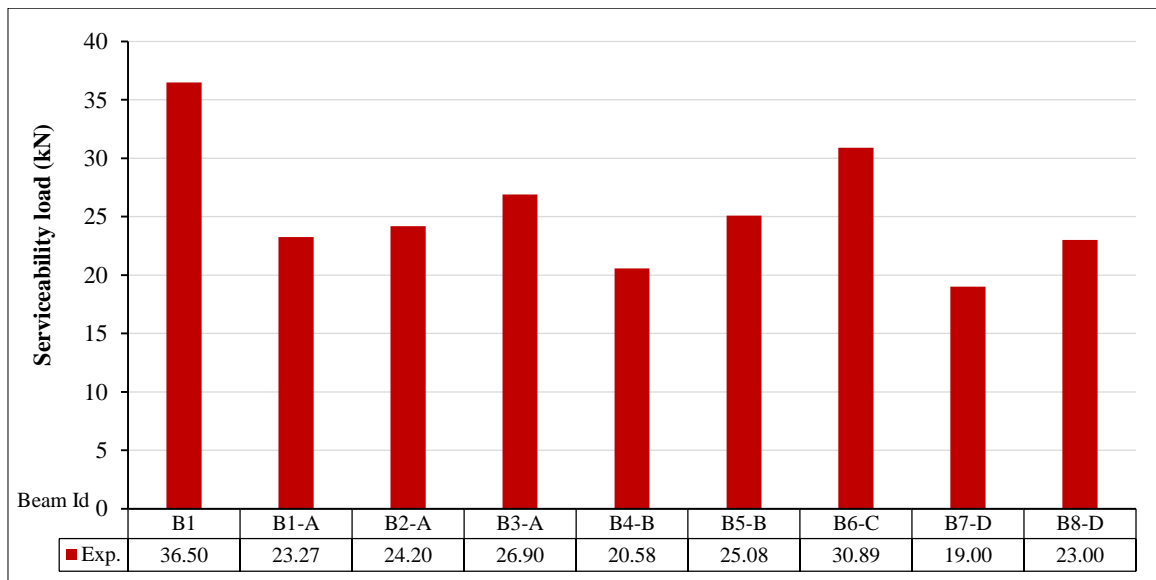


Figure 13. Serviceability load for tested beams

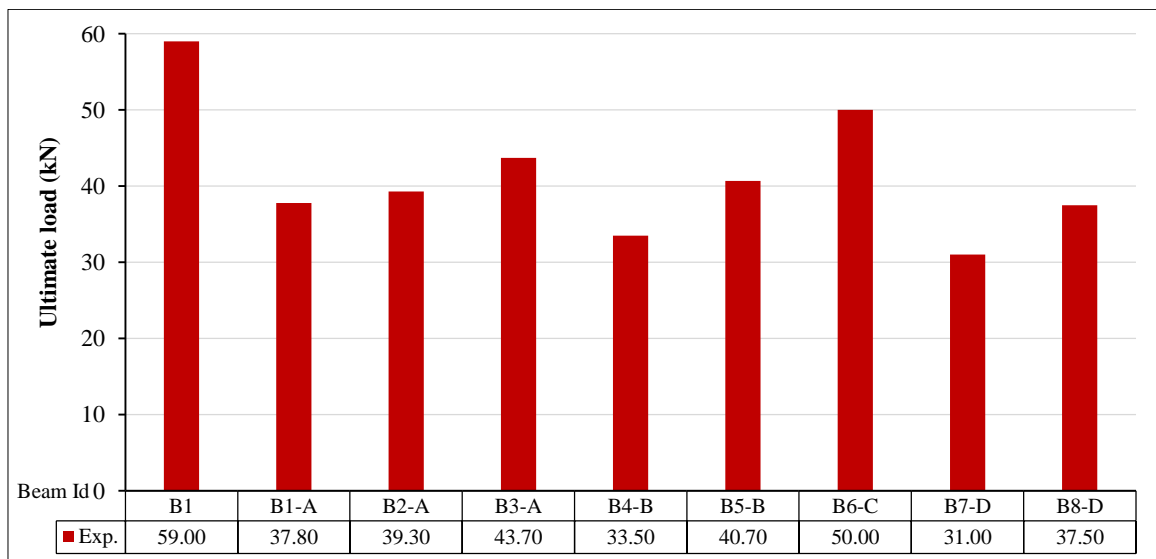


Figure 14. Ultimate load for tested beams

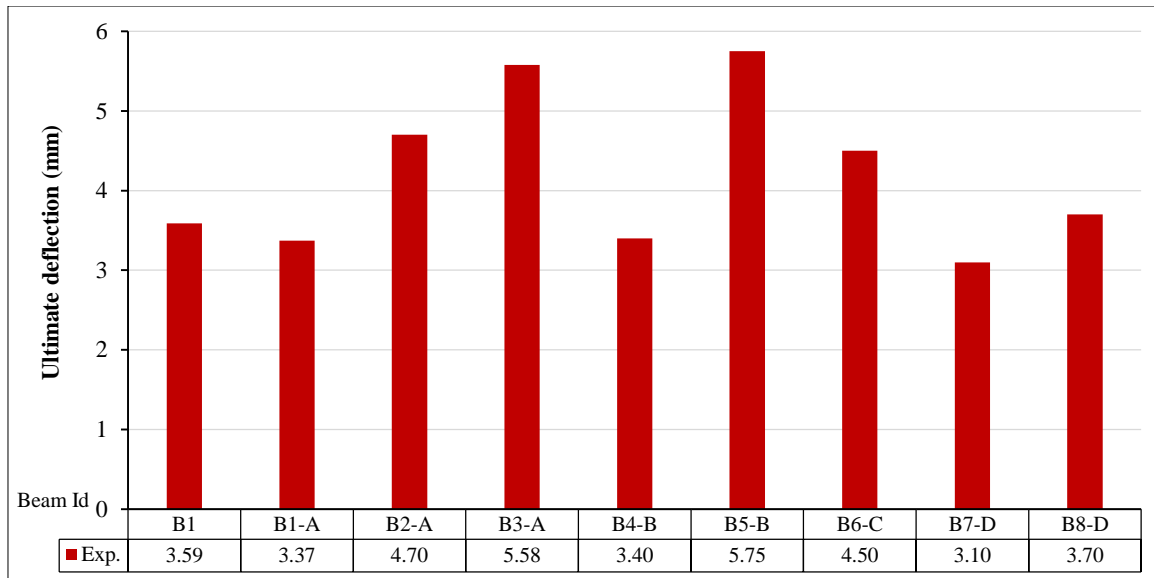


Figure 15. Ultimate deflection for tested beams

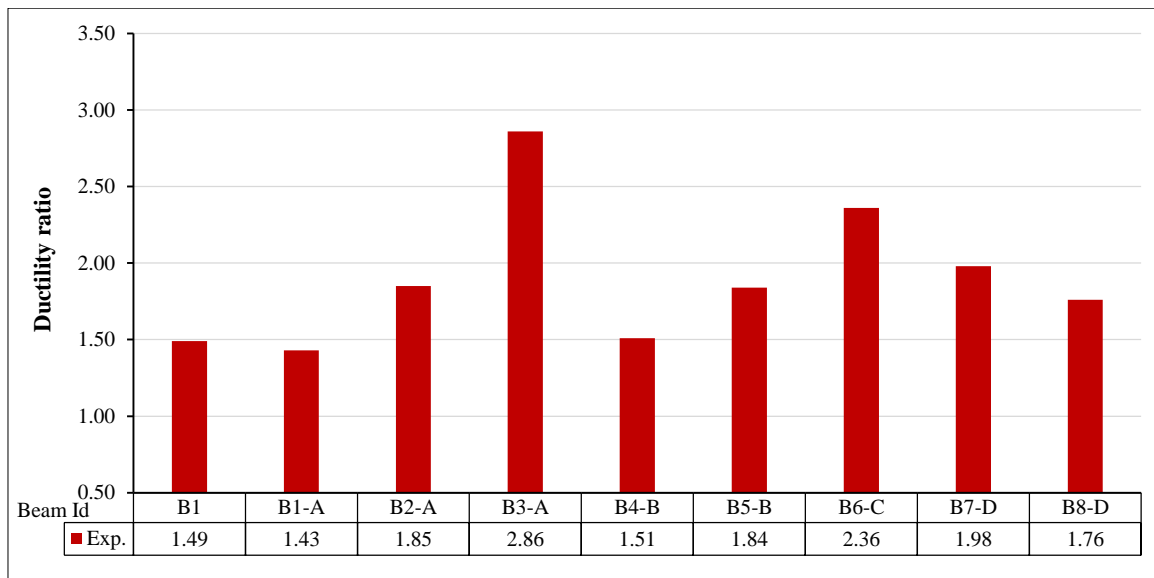


Figure 16. Ductility ratio for tested beams

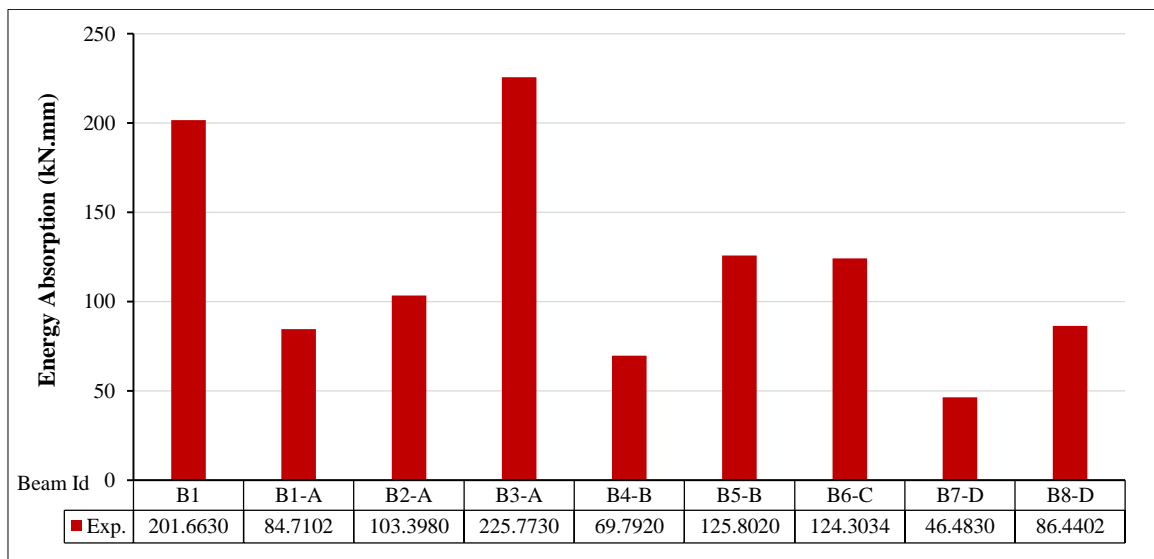


Figure 17. Energy absorption for tested beams

All these figures indicate that the beam B7-D was reinforced with two high tensile steel bars of 12 mm and 10 mm diameter on the tension side and compression side, respectively, as well as one layer of glass fiber mesh. It had the lowest first crack load and ultimate load. The beam B6-C has a high ultimate load bearing capability since it was reinforced with one layer of tensar mesh and two high tensile steel bars of 12 mm and 10 mm diameter on the tension side and the compression side, respectively.

### 3.4. Load-Strain Relationship

The load-strain curves for all examined specimens are presented in Figures 18 to 26. The connection between load and strain was practically linear up to the first cracking load, after which it began to depart from the linear relationship.

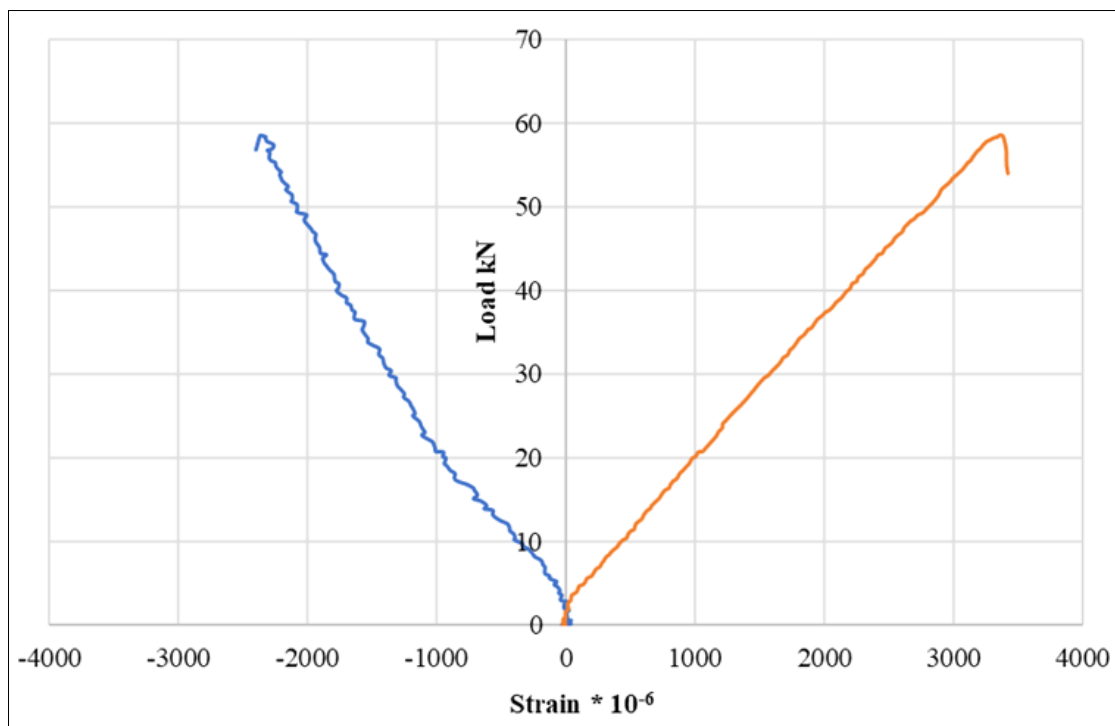


Figure 18. B1-Load-strain curve

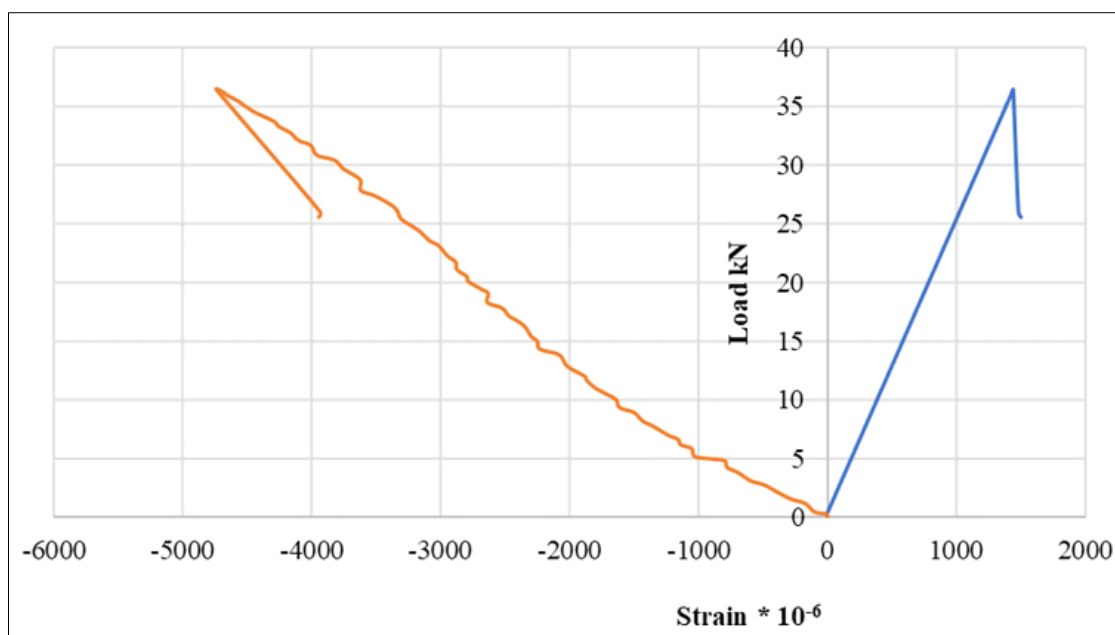


Figure 19. B1-A-Load-strain curve



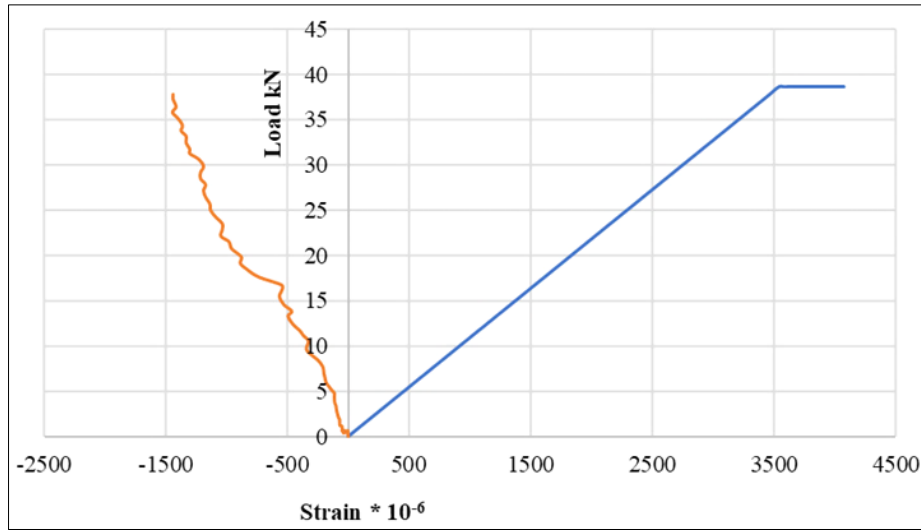


Figure 20. B2-A-Load-strain curve

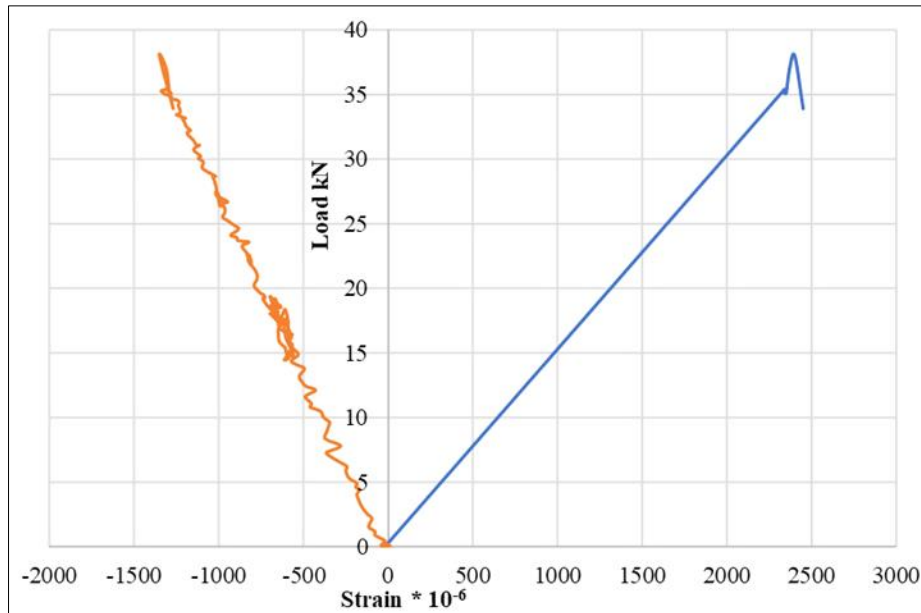


Figure 21. B3-A-Load-strain curve

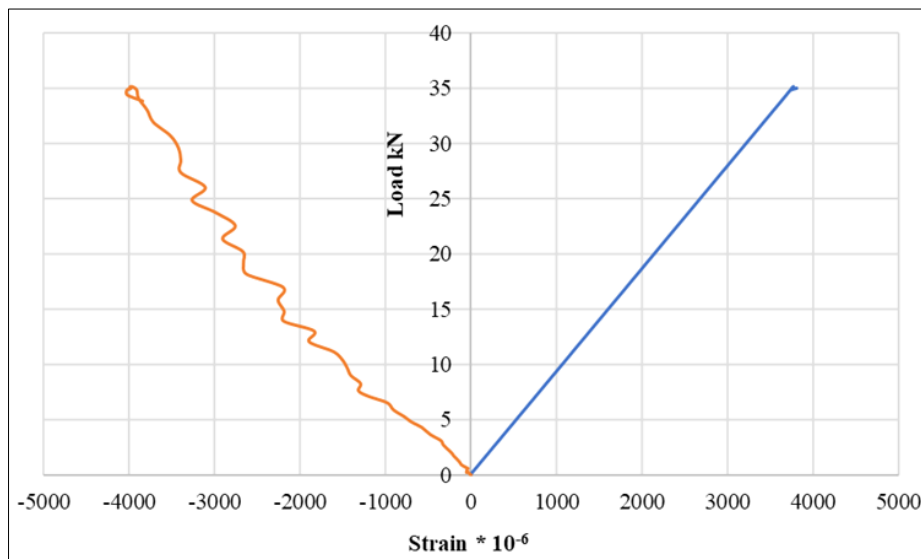


Figure 22. B4-B-Load-strain curve

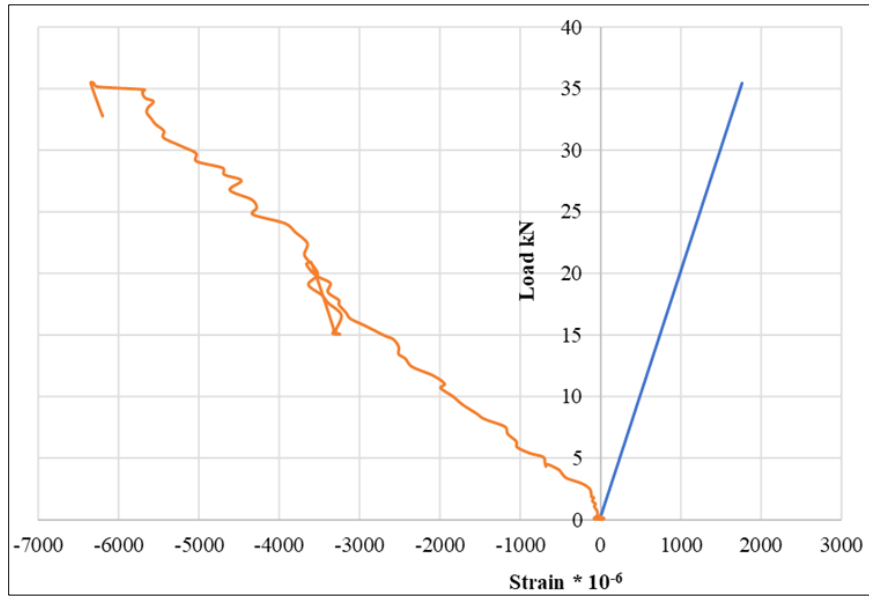


Figure 23. B5-B-Load-strain curve

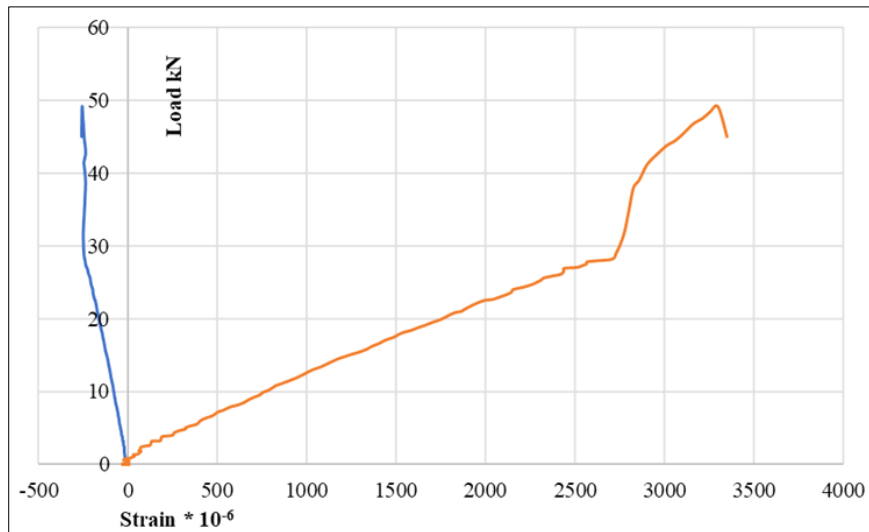


Figure 24. B6-C-Load-strain curve

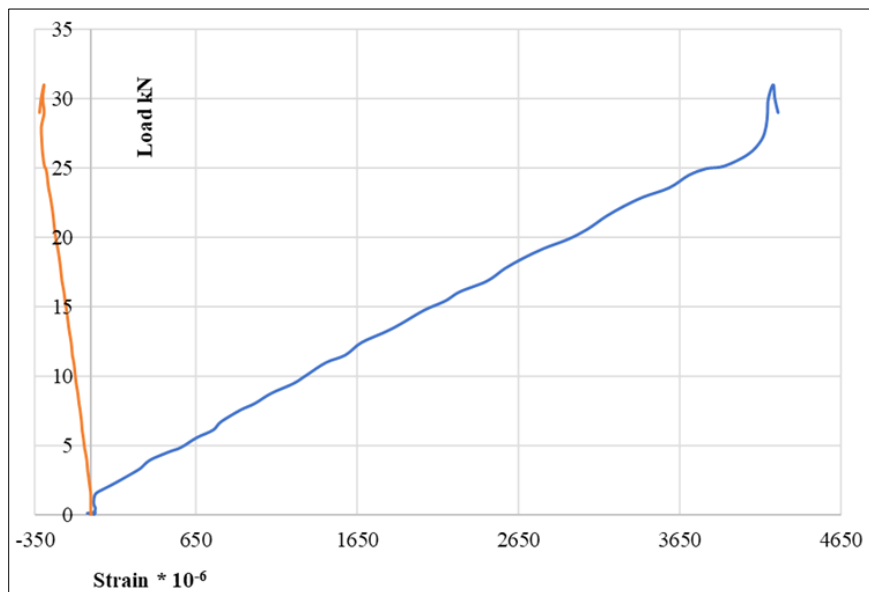


Figure 25. B7-D-Load-strain curve

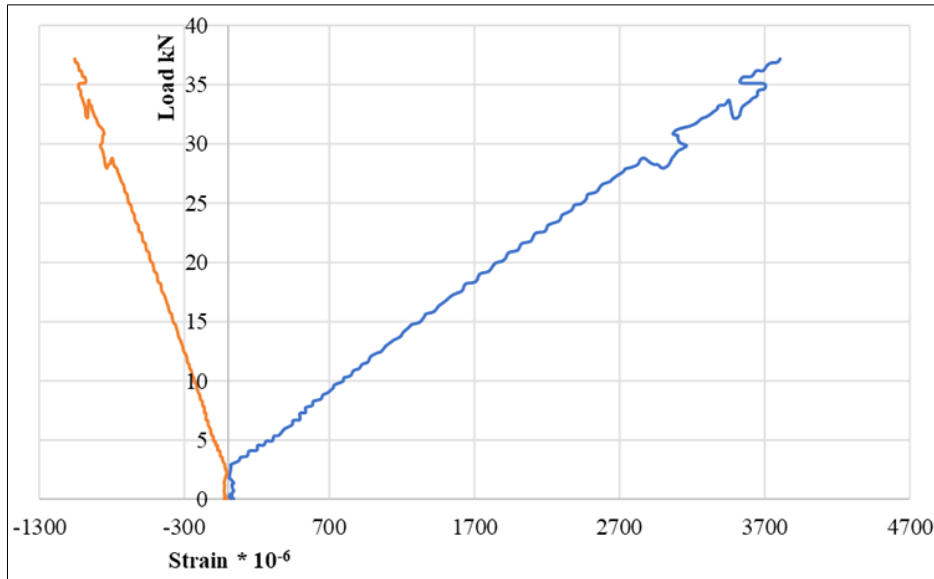


Figure 26. B8-D-Load-strain curve

#### 4. The Nonlinear Analysis (NLA)

To corroborate the outcomes of the experimental investigation, a nonlinear analysis was undertaken. Table 5 displayed the analytical findings derived with the ANSYS 2019-R1 [24] software.

Table 5. NLFEA analytical results

Beam no.	First crack load (kN)	Ultimate load (kN)	Def. at first crack load (mm)	Def. at Ult. load (mm)	Ductility ratio	Energy Absorption (kN.mm)
B1	37.80	53.10	2.16	3.23	1.50	181.497
B1-A	24.30	34.02	2.12	3.33	1.57	76.239
B2-A	17.10	35.37	2.28	4.43	1.94	93.058
B3-A	20.25	39.84	1.76	5.54	3.15	203.196
B4-B	18.00	30.15	2.02	3.33	1.65	62.183
B5-B	21.60	36.63	2.81	5.18	1.84	113.222
B6-C	20.70	45.00	1.71	4.91	2.87	111.873
B7-D	13.50	27.90	1.40	2.89	2.06	41.835
B8-D	19.80	33.75	1.89	3.66	1.94	77.796

#### 4.1. Modeling of Specimens

The performance of geopolymer ferrocement beams was evaluated using nonlinear analysis, as illustrated in Figure 27.

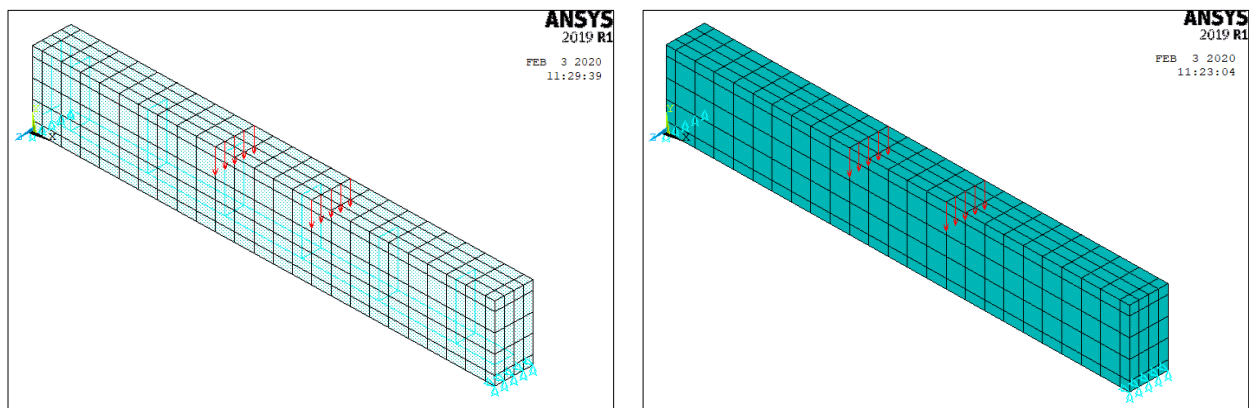


Figure 27. Modeling of beams

#### 4.1.1. Types of Elements

The concrete stress-strain curve was represented by the element Solid 65. While the reinforcing bars and reinforcing stirrups were represented by element Link 180 3-D. All ferrocement reinforcement was represented in the concrete element Solid 65 by determining the volumetric ratio (the reinforcement steel ratio to concrete). As ANSYS [24] allows the user to insert three different types of rebar materials into the concrete. Each substance is represented by x, y, and z. In the smeared model, the orientation angles represented the reinforcement orientation. As a result, as described in section, ferrocement reinforcement was represented as spread layers with a volumetric ratio (4.1.3). Element type geometry, as seen in Figure 28.

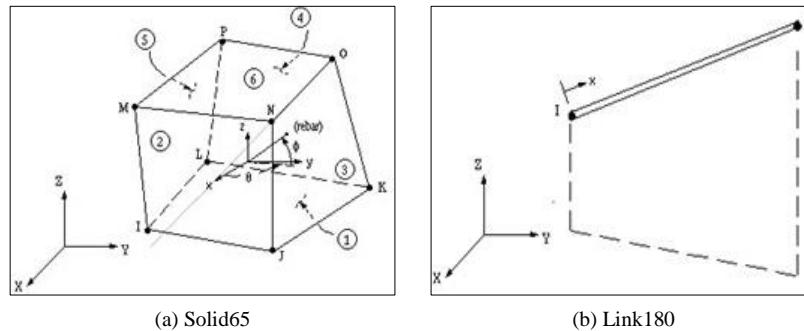


Figure 28. Element types geometry

#### 4.1.2. Real Constants

Real Constant Set 1 is used for the Solid65 element. It requires real constants for rebar, assuming a smeared model. Values can be entered for Material Number, Volume Ratio, and Orientation Angles. The material number refers to the type of material used for the reinforcement. The volume ratio refers to the ratio of steel to concrete in the element and is used for ferrocement representation. The orientation angles refer to the orientation of the reinforcement in the smeared model.

ANSYS 2019-R1 allows the user to enter three rebar materials in the concrete. Each material corresponds to x, y, and z directions in the element (Figure 28). The reinforcement has uniaxial stiffness, and the directional orientation is defined by the user. In the present study, the beam is modeled using discrete reinforcement. Real Constant Sets 2 and 3 are defined for the Link8 element. Values for cross-sectional area and initial strain were entered. Cross-sectional areas in sets 2 and 3 refer to the main and secondary reinforcement, respectively.

#### 4.1.3. Material Properties

This part shows the material properties for concrete, reinforcing steel bars, and reinforcing expanded and welded wire mesh.

- The material properties for concrete:
  - Elastic modulus of elasticity ( $E_c = 4400 \sqrt{f_{cu}} = 24100 \text{ N/mm}^2$ ) [28].
  - Poisson's ratio ( $\nu = 0.3$ ) [28].
- The material properties for reinforcing steel bars:
  - Elastic Modulus of elasticity ( $E_s = 200 \text{ kN/mm}^2$ ) [28].
  - Yield stress ( $f_y = 400 \text{ N/mm}^2$  &  $f_{y_{st}} = 240 \text{ N/mm}^2$ ) [28].
  - Poisson's ratio ( $\nu = 0.2$ ) [28].
  - Area of steel of  $\phi 12$  ( $A_s = 112 \text{ mm}^2$ )
  - Area of steel of  $\phi 8$  ( $A_s = 50.3 \text{ mm}^2$ )
- The properties for welded wire mesh:
  - Volumetric ratio of one layer = 0.0027
  - Volumetric ratio of two layers = 0.0054
  - Volumetric ratio of three layers = 0.0081
- The material properties for Expanded wire mesh:
  - Volumetric ratio of one layer = 0.00753
  - Volumetric ratio of two layers = 0.01510
- The material properties for tensar mesh:



Volumetric ratio of one layer = 0.02040

- The material properties for Glass fiber mesh:

Volumetric ratio of one layer = 0.00535

Volumetric ratio of two layers = 0.01070

#### 4.1.4. Modeling Methodology

A full beam is used for modeling with proper boundary conditions. Ideally, the bond strength between the concrete and steel reinforcement should be considered. However, in this study, a perfect bond between materials is assumed. The beam was modeled as a volume.

#### 4.1.5. Meshing

To obtain good results from the Solid65 element, the use of a rectangular mesh is recommended. Therefore, the mesh was set up such that square or rectangular elements were created. This properly sets the width and length of elements in the plates to be consistent with the elements and nodes in the concrete portions of the model. The overall mesh of the concrete volumes is shown in Figure 27.

#### 4.1.6. Analysis Type

The finite element model for this analysis is a simple beam. For the purposes of this model, the static analysis type is utilized. The Sol'n Controls command dictates the use of a linear or non-linear solution for the finite element model. Table 5 shows the finite element data, including first crack load, ultimate load, deflection at first crack and ultimate load, ductility ratio, and energy absorption.

#### 4.1.7. Ultimate Load

Table 5 shows the first fracture loads and ultimate loads for modeled beams. Control B1 has an ultimate load of 53.10 kN. The ultimate loads of group A, beams B1-A to B3-A, ranged from 34.02 kN to 39.84 kN. The ultimate loads for group B, beams B4-B and B5-B, are 30.15 kN and 36.63 kN, respectively. The ultimate load of the modeled beams was enhanced by using both fibers. Beam B6-C for group C, having an ultimate load of 45.00 kN. The ultimate loads for group D, beams B7-D and B8-D, were 27.90 kN and 33.75 kN, respectively.

#### 4.1.8. Ultimate deflection

The ultimate deflection for all modeled beams is shown in Table 5. The control B1 had a center deflection of 3.23 mm. The greatest central deflection for group A varied from 3.33 mm to 5.54 mm for beams B1-A to B3-A, which was more than that of control B1. The greatest central deflection at ultimate load for beams B4-B and B5-B in group B was 3.33 mm and 5.18 mm, respectively, which was likewise more than that of control beam B2. Beam B6-C for group C, having an ultimate deflection of 4.91 mm. The ultimate deflections for group D, beams B7-D and B8-D, were 2.89 and 3.66 mm, respectively.

## 5. Experimental and Analytical Findings Comparisons

The comparison of experimental and analytical data confirms that the non-linear models gathered represent the response of geopolymers ferrocement RC beams in terms of first crack load, ultimate load, first crack and ultimate displacement, and crack patterns.

### 5.1. Ultimate Load

The ultimate failure experimental load and the analytical load were compared in Table 6 and Figure 29. The experimental and analytical ultimate loads are in good agreement.

**Table 6. Experimental and analytical Results**

Beam no.	First crack load	First crack load	Ultimate load	Ultimate load	Def. at Ult. load	Def. at Ult. load
	(kN)	(kN)	(kN)	(kN)	(mm)	(mm)
	NLA.	EXP.	NLA.	EXP.	NLA.	EXP.
B1	37.80	42.0	53.10	59.0	3.23	3.59
B1-A	24.30	27.0	34.02	37.8	3.33	3.37
B2-A	17.10	19.0	35.37	39.3	4.43	4.70
B3-A	20.25	22.5	39.84	43.7	5.54	5.58
B4-B	18.00	20.0	30.15	33.5	3.33	3.40
B5-B	21.60	24.0	36.63	40.7	5.18	5.75
B6-C	20.70	23.0	45.00	50.0	4.91	4.50
B7-D	13.50	15.0	27.90	31.0	2.89	3.10
B8-D	19.80	22.0	33.75	37.5	3.66	3.70

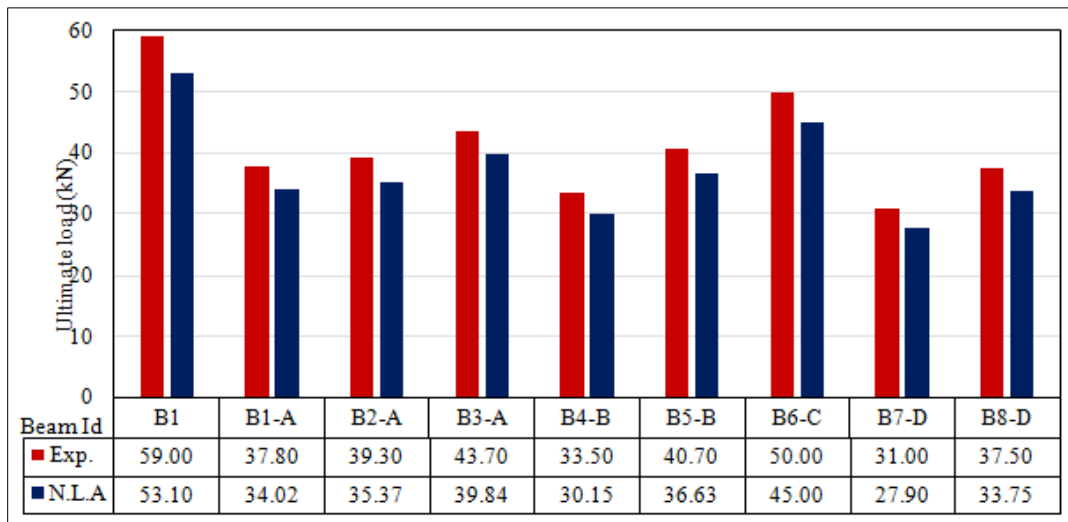


Figure 29. Comparison between Exp. & NLA ultimate loads

5.2. Ultimate Displacement

The ultimate experimental displacement and the analytical displacement were compared in Figure 30 and Table 6. The load-displacement curves for experimental and modelled beams, as shown in Figures 30 to 39, agreed well in terms of control beam deflection

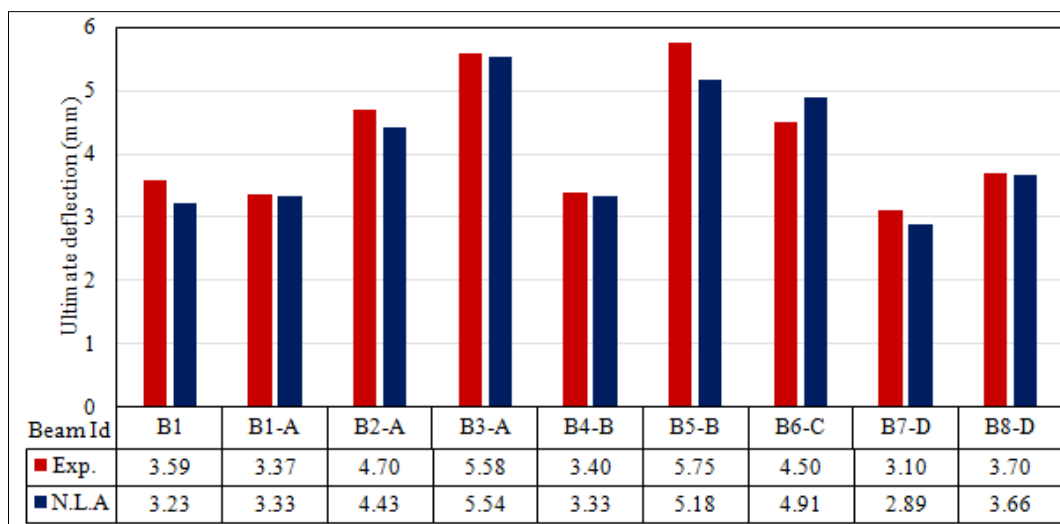


Figure 30. Comparison between Exp. & NLA ultimate deflections

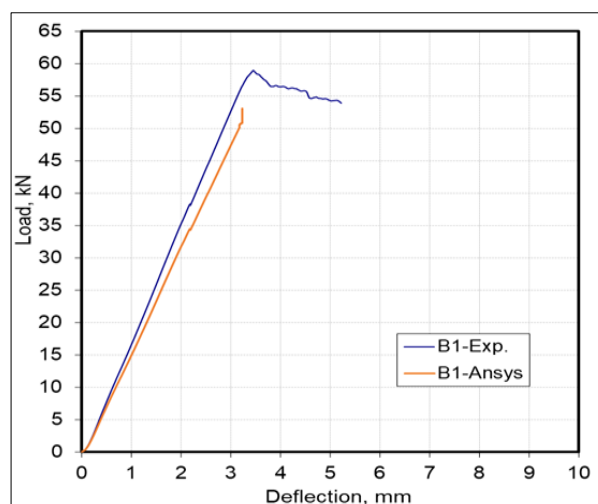


Figure 31. B1-Load central deflection curve

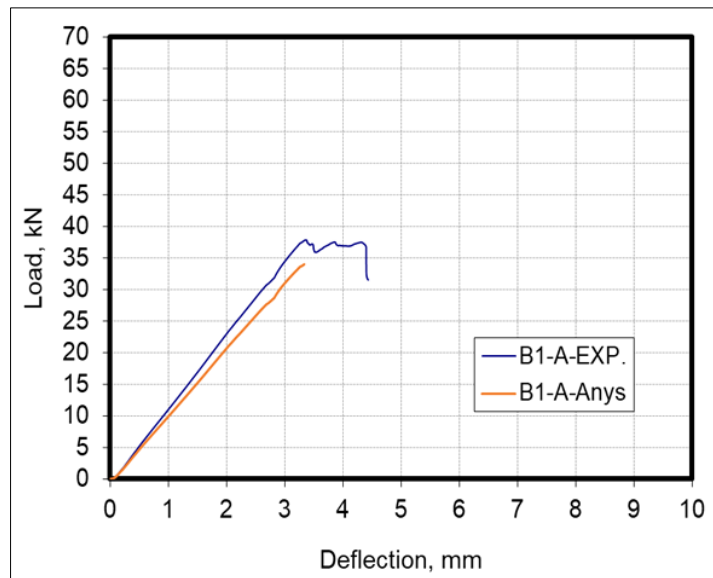


Figure 32. B1-A-Load central deflection curve

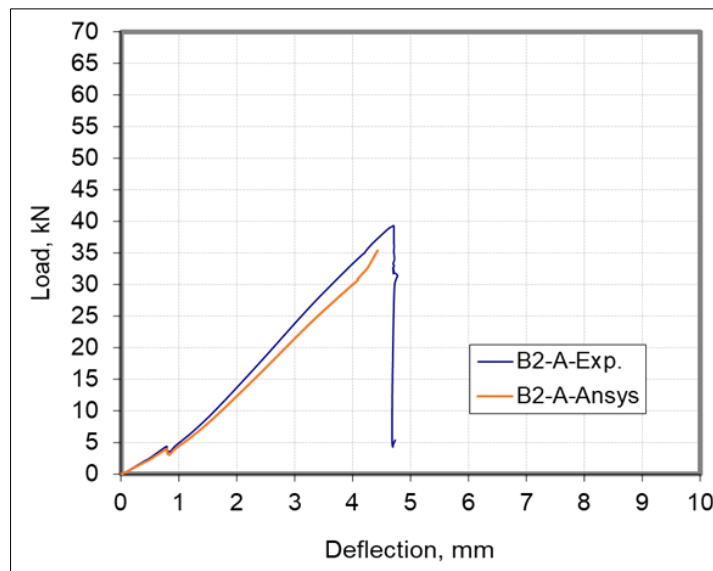


Figure 33. B2-A-Load central deflection curve

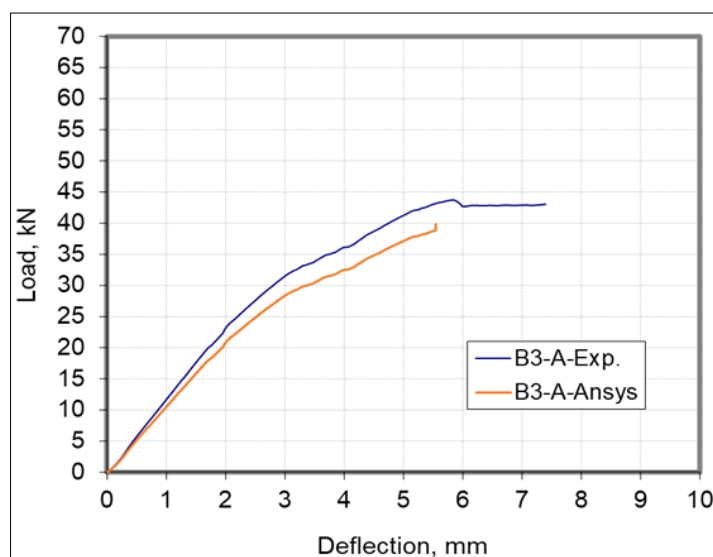


Figure 34. B3-A-Load central deflection curve

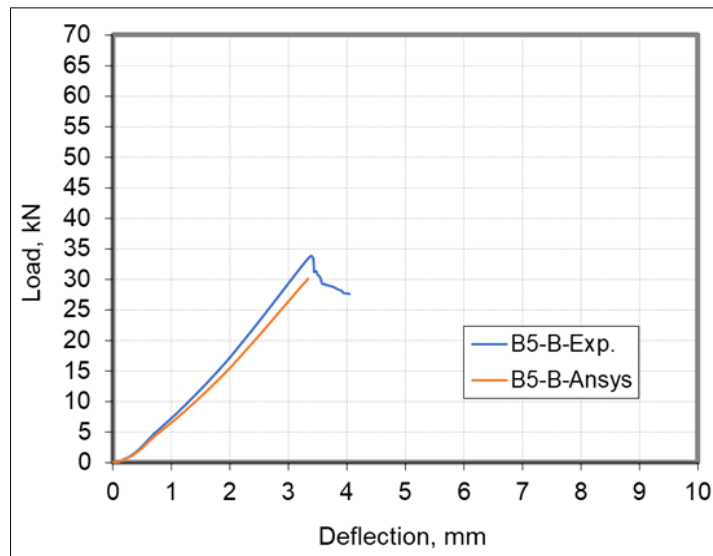


Figure 35. B4-B-Load central deflection curve

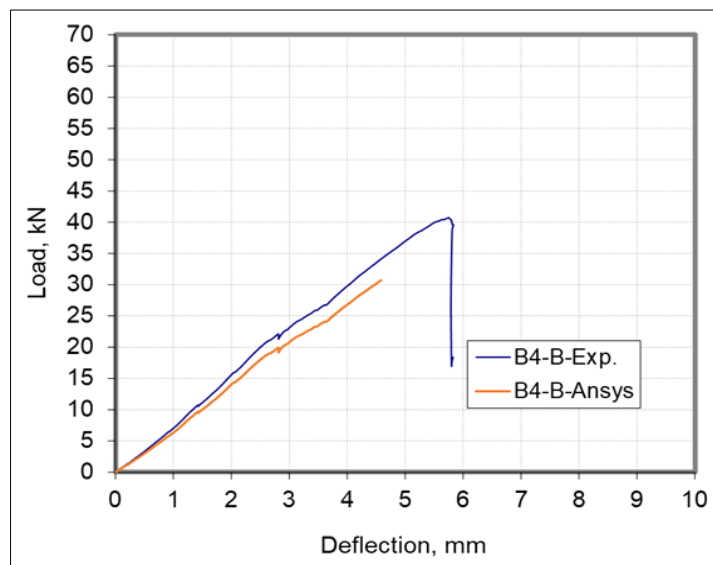


Figure 36. B5-B-Load central deflection curve

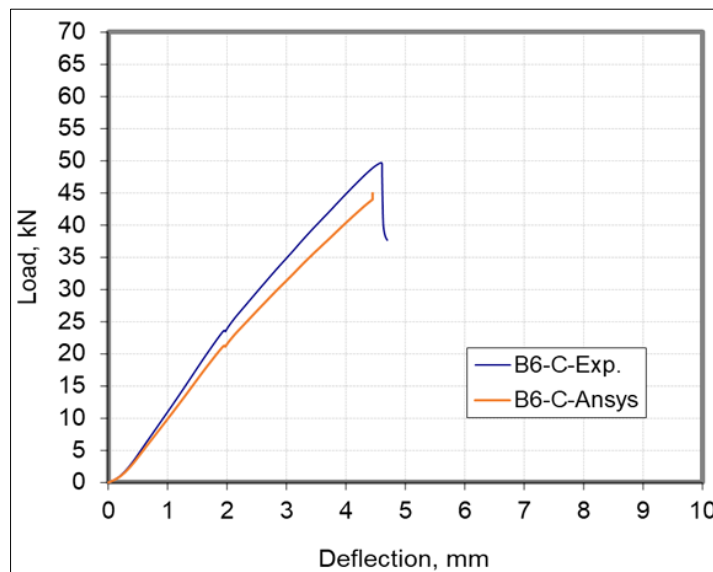


Figure 37. B6-C-Load central deflection curve



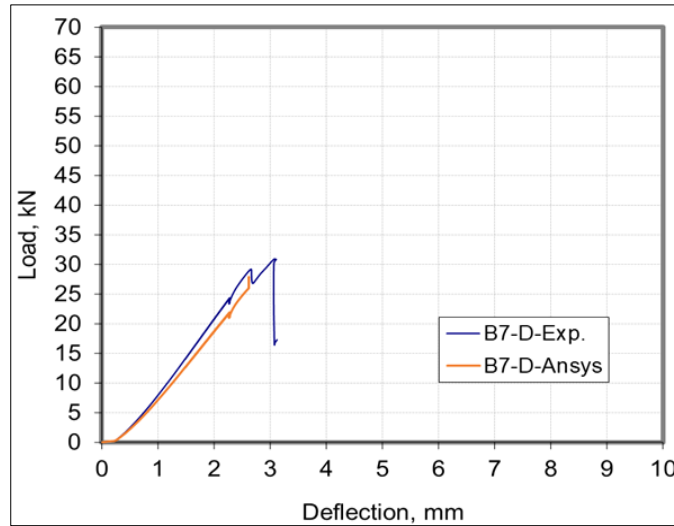


Figure 38. B7-D-Load central deflection curve

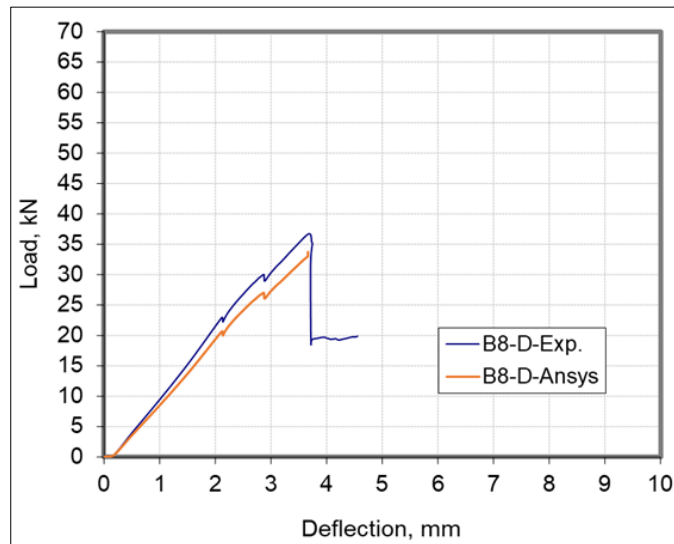


Figure 39. B8-D-Load central deflection curve

### 5.3. Energy Absorption

The experimental and analytical energy absorption was found to be in good agreement in Figure 40. Both experimental and analytical energy absorption values were high for beams B3-A, B6-C, and B7-D.

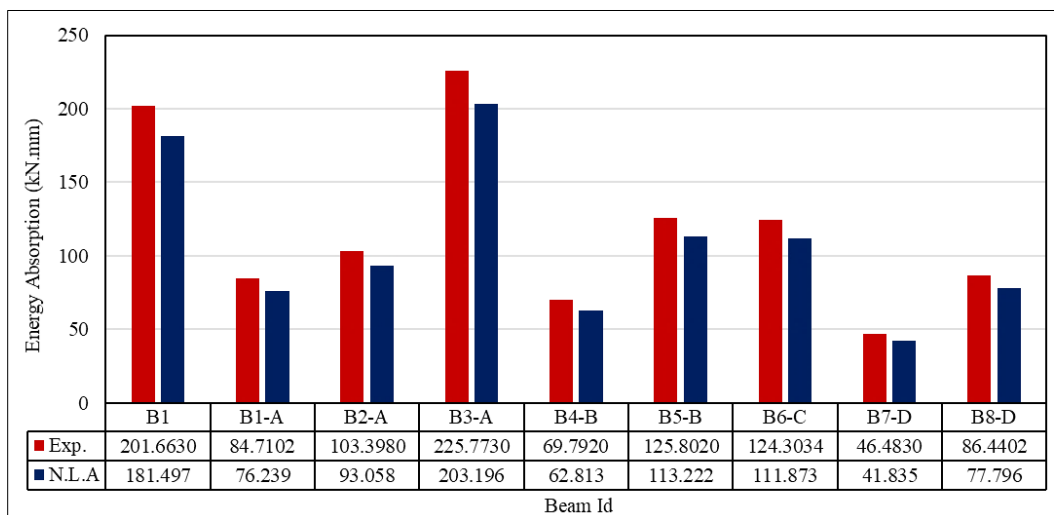


Figure 40. Comparison between Exp. & NLA energy absorption

### 5.4. Cracking Patterns

The cracking pattern for designation (Control beam) is depicted in Figure 41. This image indicates that flexural fractures occurred at both edges of the specimen B1. As the load increased, the fractures spread diagonally, resulting in the formation of additional flexural cracks. The cracks began to spread vertically near the specimen's mid-span.

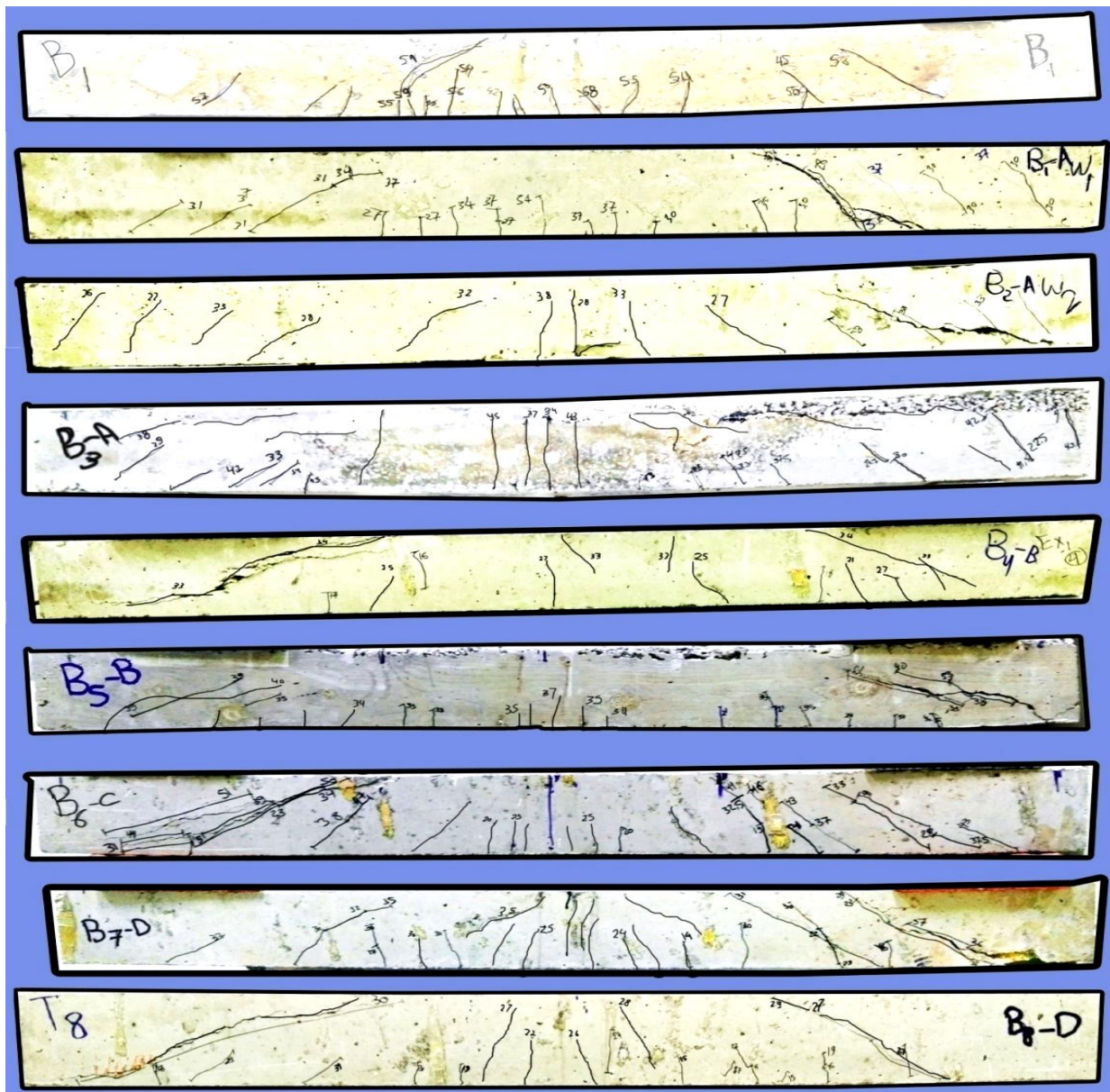


Figure 41. Experimental crack patterns

The first crack appeared in the center of the beam for test specimens from group (A). As seen in Figure 18. As the stress grew, fresh fractures sprang on both sides of the beam, while the primary crack moved upwards. As the weight was increased further, fresh angled fissures formed at the beam's borders. These fracture growth patterns persisted until the beam failed. According to this figure, the crack width is greater than in the control beams. Cracks appeared all over the beam. As demonstrated in Figure 18, the crack distribution for designation (B) was slightly different from the preceding designations. The figure demonstrates that few flexural fractures emerged in the middle of the specimens and did not propagate to the top surface, whereas cracks developed towards the end of the specimens and did propagate to the top surface. It was discovered that the fracture width is narrower than that of the group (A). The first crack developed along the side of the beam for test specimens from groups (C & D), as illustrated in Figure 18. When the weight was raised, additional cracks appeared on both sides of the initial crack. The crack width in the control beams is greater.

The cracking patterns acquired from experimental and nonlinear studies were shown in Figure 42.

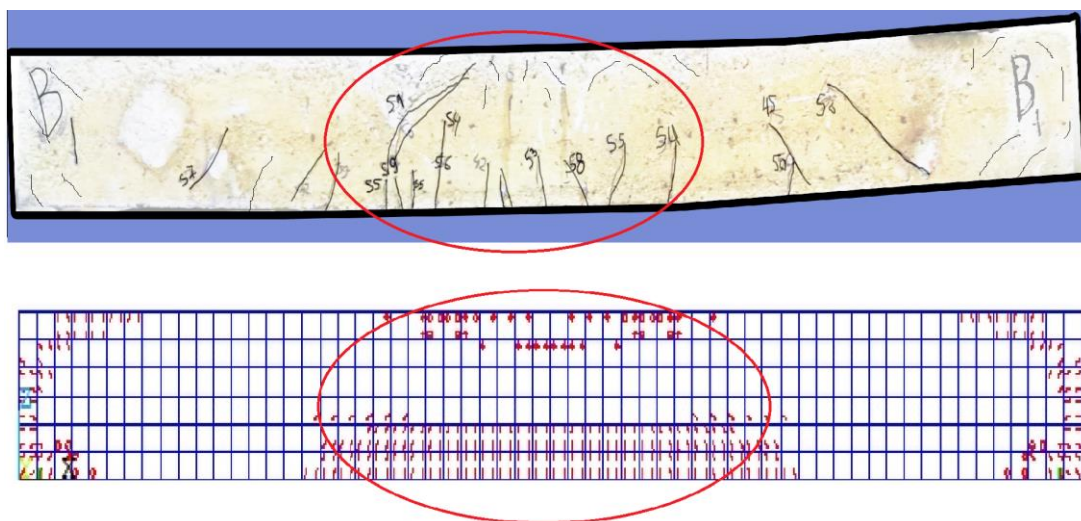


Figure 42. Cracks spread for control specimen

## 6. Conclusions

In this paper, the structural performance of GGBS-based geopolymer ferrocement beams was investigated experimentally and numerically. The primary influencing factors are the kind of expanded and welded steel mesh and tensor mesh and the number of layers. The experimental study included nine samples of 150 mm in height, 75 mm in width, and 1700 mm in length of geopolymer ferrocement beams that were evaluated under flexural pressure to failure. The study also investigated the effect of some variables, such as ultimate loads, displacement, cracking behavior, and ductility. Using ANSYS-19 software, nonlinear finite element analysis (NLFEA) was carried out to demonstrate the behavior of composite ferrocement geopolymer beams. The ensuing experimental and numerical data demonstrated that the degree of experimental value estimation supplied by the FE simulations was sufficient. Based on the results obtained, it was concluded that:

- The ultimate loads of the tensor ferrocement tested specimens were reduced by around 15% in comparison to control specimens.
- The first cracks, ultimate loads, energy absorption, and ductility index enhanced as the volume percent of the wire mesh reinforcement increased.
- Utilizing expanded & welded steel mesh, tensor mesh, and fiber glass mesh for durability purposes might reduce the overall weight of the reinforcing steel. The weight of the steel was reduced by 20% to 30%.
- In comparison to using welded or expanded steel mesh, the ultimate load was reduced by around 38% when fiber glass mesh was used as reinforcement.
- Ferrocement geopolymer beams outperformed steel reinforced concrete control beams in terms of first crack load, serviceability load, ultimate load, ductility, and energy absorption.
- When compared to the steel geopolymer beams, the ferrocement geopolymer beams had more cracks with narrower widths.
- The analytical results differ by an average of 4% when comparing the numerical and experimental ductility ratios and energy absorption measurements.
- The analytical approaches for computing the first crack and ultimate load yield good predictions for these loads and the failure mechanisms of the beams. As a result, improved strength, deformation properties, and cracking behavior with significant reinforcement savings.
- Apart from the anticipated economic and environmental benefits, proven ferrocement geopolymer beams might be effectively employed as a substitute to existing geopolymer RC beams in both developed and developing nations.

## 7. Declarations

### 7.1. Author Contributions

Conceptualization, T.A.E. and A.F.D.; methodology, T.A.E., H.H.A., and A.K.Y.; software, T.A.E. and Y.B.S.; validation, T.A.E. and A.F.D.; resources, H.H.A. and A.K.Y.; data curation, Y.B.S.; writing—original draft preparation, T.A.E. and A.K.Y.; writing—review and editing, T.A.E., Y.B.S., and A.K.Y.; supervision, T.A.E., H.H.A., and Y.B.S.; project administration, Y.B.S. All authors have read and agreed to the published version of the manuscript.



## 7.2. Data Availability Statement

The data presented in this study are available in the article.

## 7.3. Funding

The authors received no financial support for the research, authorship, and/or publication of this article.

## 7.4. Conflicts of Interest

The authors declare no conflict of interest.

## 8. References

- [1] Fahmy, E., & Shaheen, Y. (1994, June). Laminated ferrocement for strengthening and repairing of reinforced concrete beams. Proceedings of the annual conference of the Canadian society for civil engineering, 1-4 June, 1994, Winnipeg, Canada.
- [2] Shah, S. P., & Namman, A. E. P. (1971). Tensile Tests of Ferrocement. *ACI Journal*, 68, 693-698. doi:10.14359/7233.
- [3] Mays, G. C., & Barnes, R. A. (1995). Ferrocement permanent formwork as protection to reinforced concrete. *Journal of Ferrocement*, 25(4), 331–345.
- [4] Abdul Kadir, M., Abdul Samad, A., Che Muda, Z., & Ali, A. (1997). Flexural Behavior of Composite Beam with ferrocement Permanent Formwork. *Journal of Ferrocement*, 27(3), 209–214.
- [5] Fahmy, E. H., Shaheen, Y. B., Abou Zeid, M. N., & Gaafar, H. (2004). Development of ferrocement panels for floor and wall construction. 5<sup>th</sup> Structural Specialty Conference of the Canadian Society for Civil Engineering, 2-5 June, 2004, Saskatoon, Canada.
- [6] Fahmy, E. H., Shaheen, Y. B. I., & El-Dessouki, W. M. (1995). Application of Ferrocement for Construction. *Journal of Ferrocement*, 25(2), 115.
- [7] Swamy, R. N., & Shaheen, Y. B. I. (1990). Tensile Behavior of Thin Ferrocement Plates. (1990). SP-124: Thin Section Fiber Reinforced Concrete and Ferrocement. doi:10.14359/2828.
- [8] National Academy of Sciences. (1973). Ferrocement: Applications in Developing Countries. A Report of an Adhoc Panel of the Advisory Committee on Technological Innovation Board on Science and Technology for International Development Office of the Foreign Secretary, Washington, United States.
- [9] Joshi, A. D. (1974). Strength and Behavior of Ferrocement Load Bearing Wall Elements. Ph.D. Thesis, Bangalore, India.
- [10] El-Sayed, T. A., & Erfan, A. M. (2018). Improving shear strength of beams using ferrocement composite. *Construction and Building Materials*, 172, 608–617. doi:10.1016/j.conbuildmat.2018.03.273.
- [11] Rao, G. S., & Kumar, B. S. C. (2019). Experimental investigation of GGBS based geopolymer concrete with steel fibers. *International Journal of Recent Technology and Engineering (IJRTE)*, 7(6C2), 49-55.
- [12] Saranya, P., Nagarajan, P., & Shashikala, A. P. (2021). Performance Studies on Steel Fiber–Reinforced GGBS-Dolomite Geopolymer Concrete. *Journal of Materials in Civil Engineering*, 33(2), 4020447. doi:10.1061/(asce)mt.1943-5533.0003530.
- [13] Islam, A., Alengaram, U. J., Jumaat, M. Z., Ghazali, N. B., Yusoff, S., & Bashar, I. I. (2017). Influence of steel fibers on the mechanical properties and impact resistance of lightweight geopolymer concrete. *Construction and Building Materials*, 152, 964–977. doi:10.1016/j.conbuildmat.2017.06.092.
- [14] Erfan, A. M., Abd Elnaby, R. M., Elhawary, A., & El-Sayed, T. A. (2021). Improving the compressive behavior of RC walls reinforced with ferrocement composites under centric and eccentric loading. *Case Studies in Construction Materials*, 14, 541. doi:10.1016/j.cscm.2021.e00541.
- [15] Prabu, B., Kumutha, R., & Vijai, K. (2017). Effect of fibers on the mechanical properties of fly ash and GGBS based geopolymer concrete under different curing conditions. *Indian Journal of Engineering and Materials Sciences*, 24, 5–12.
- [16] Jayarajan, G., & Arivalagan, S. (2020). An experimental studies of geopolymer concrete incorporated with fly-ash & GGBS. *Materials Today: Proceedings*, 45, 6915–6920. doi:10.1016/j.matpr.2021.01.285.
- [17] Al-Majidi, M. H., Lampropoulos, A., & Cundy, A. B. (2017). Steel fibre reinforced geopolymer concrete (SFRGC) with improved microstructure and enhanced fibre-matrix interfacial properties. *Construction and Building Materials*, 139, 286–307. doi:10.1016/j.conbuildmat.2017.02.045.
- [18] Kuranlı, Ö. F., Uysal, M., Abbas, M. T., Cosgun, T., Niş, A., Aygörmez, Y., Canpolat, O., & Al-mashhadani, M. M. (2022). Evaluation of slag/fly ash based geopolymer concrete with steel, polypropylene and polyamide fibers. *Construction and Building Materials*, 325, 126747. doi:10.1016/j.conbuildmat.2022.126747.



- [19] Lao, J. C., Xu, L. Y., Huang, B. T., Dai, J. G., & Shah, S. P. (2022). Strain-hardening Ultra-High-Performance Geopolymer Concrete (UHPGC): Matrix design and effect of steel fibers. *Composites Communications*, 30, 101081. doi:10.1016/j.coco.2022.101081.
- [20] Nassif, H. H., & Najm, H. (2004). Experimental and analytical investigation of ferrocement–concrete composite beams. *Cement and Concrete Composites*, 26(7), 787-796. doi:10.1016/j.cemconcomp.2003.08.003.
- [21] El-sayed, T. A. (2021). Axial compression behavior of ferrocement geopolymer HSC columns. *Polymers*, 13(21), 3789. doi:10.3390/polym13213789.
- [22] El-Sayed, T. A., Shaheen, Y. B., AbouBakr, M. M., & Abdelnaby, R. M. (2022). Behavior of ferrocement water pipes as an alternative solution for steel water pipes. *Case Studies in Construction Materials*, e01806. doi:10.1016/j.cscm.2022.e01806.
- [23] ECP 203-2020. (2020). Egyptian Code of Practice: Design and Construction for Reinforced Concrete Structures. Egyptian, Ministry of Housing, Cairo, Egypt.
- [24] ANSYS. (2019). Engineering Analysis system user's Manual. Ansys, Engineering Simulation Software, San Jose, United States.